Mixing of cogenetic magmas in the Cretaceous Zhangzhou calc-alkaline granite from southeast China recorded by in-situ apatite geochemistry

XIAOBING ZHANG[1,2,†], FENG GUO[1,*], BO ZHANG[1,2], LIANG ZHAO[1], AND GUOQING WANG[1,2]

[1]State Key Laboratory of Isotope Geochemistry, Guangzhou Institute of Geochemistry, Chinese Academy of Sciences, Guangzhou 510640, China
[2]College of Earth and Planetary Sciences, University of Chinese Academy of Sciences, Beijing 100049, China

ABSTRACT

Mixing of cogenetic magmas represents an important process in granite petrogenesis but is difficult to identify and is consequently often overlooked due to the absence of obvious isotopic distinctions between the mixed melts. We have conducted in situ elemental and O isotope analyses on apatite from Cretaceous Zhangzhou calc-alkaline granite in southeast China. We integrated these data with micro-analyses on other minerals (plagioclase, zircon, and titanite) as well as whole-rock geochemistry to decipher the mixing history of this granitic complex. The apatite occurs as an early crystallizing phase forming inclusions in biotite, plagioclase, and titanite, and is characterized by core-rim zonation textures with a dark core and bright rims in backscattered images. The core domains have remarkably higher SO_3 and Li concentrations but much lower SiO_2, REE, and Y concentrations than the rim domains. However, both the cores and rims show geochemical compositions similar to that from typical I-type granite and also have mantle-like O isotope compositions (the core has $\delta^{18}O$ = 5.3–6.8‰ and the rim has $\delta^{18}O$ = 5.2–6.4‰, respectively), indicating crystallization from granitic melts derived from newly accreted crust. The combined major and trace element and O isotope compositions of apatite and whole-rock geochemistry suggest that compositional evolution of the Zhangzhou granite involved mixing between two cogenetic magma batches, with variable degrees of subsequent differentiation. Batch I magma was a low-SiO_2 and high-SO_3 melt, whereas Batch II magma was a high-SiO_2 and low-SO_3 melt that experienced devolatilization. The high-S content in apatite cores further suggests the parental magma of the Zhangzhou granite likely originated from a sulfur-rich source comprising mainly newly accreted arc crust in response to subduction of the paleo-Pacific Ocean. The geochemical records of these magmatic processes are rarely observed in coeval zircon, titanite, and plagioclase. Our study, therefore, demonstrates that apatite geochemistry is potentially a more suitable monitor of complex magmatic evolution, including devolatilization and mixing of isotopically indistinguishable magmas.

Keywords: Apatite geochemistry, mixing, devolatilization, cogenetic magmas, Cretaceous, SE China

INTRODUCTION

Granitic rock (hereafter simply referred to as granite) is a major constituent of the upper continental crust and contains abundant mineral resources essential for sustained economic development. The compositions of granite vary extensively and can be broadly divided into I-, S-, M-, and A-type based on geochemical features and melting sources (Chappell and White 1974; Whalen et al. 1987). Many petrogenetic hypotheses, e.g., fractional crystallization, assimilation via fractional crystallization (AFC) (DePaolo 1981), and magma mixing (Griffin et al. 2002), have been proposed to interpret the geochemical diversity of granite. Nevertheless, it remains difficult to fully understand the magmatic evolution of granite since clear geochemical evidence for many hypothesized petrogenetic processes is lacking.

Recent techniques in studying chemistry and isotopic composition of minerals such as plagioclase, titanite, zircon, and apatite have become widely used petrogenetic tools in supplementing or even replacing conventional bulk-rock analyses (e.g., Streck 2008; Lisowiec et al. 2015; Nathwani et al. 2020). However, the sensitivity or applicability of these minerals in tracking magmatic processes is extremely variable because they each partition (or exclude) elements (or isotopes) of specific geochemical behavior and are typically relevant to only parts of a given crystallization sequence. Minerals that indelibly record geochemical proxies of changing magma compositions over a wide crystallization interval are rare.

Apatite is one such mineral, containing measurable concentrations of a range of elements of various geochemical behavior, including halogens, S, rare earth elements (REEs), Sr, and Y (Ayers and Watson 1993; Pan and Fleet 2002; Marks et al. 2012; Harlov 2015; Webster and Piccoli 2015; Bruand et al. 2017), that are sensitive to specific magmatic/petrogenetic processes. For example, the textural and compositional variations in apatite from the Pingtan complex in southeast (SE) China records both magmatic evolution and post-crystallization fluid activity regardless of a narrow range in Nd isotopic composition (Zhang et al. 2020). As a near-liquidus phase, apatite crystallizes early in metaluminous felsic magma (Piccoli and Candela 2002; Webster

and Piccoli 2015) and hence records early high-temperature magma compositional variations. Subsequent changes in magma composition can be reflected in compositional zonations of apatite because of insignificant intracrystalline elemental diffusion, especially for REE, S, and Si (e.g., Dowty 1980; Tepper and Kuehner 1999; Cherniak 2010). Accordingly, apatite may have significant advantages in terms of deciphering magmatic evolution trends and processes compared with other commonly used minerals such as plagioclase, titanite, and zircon.

In this contribution, we present detailed petrographic observations and systematic in situ geochemical analyses (major and trace element compositions and O and Sr isotopes) on apatite, zircon, titanite, and plagioclase from granite of Zhangzhou igneous complex, SE China. These new data, together with whole-rock geochemistry, provide a fresh perspective on the role of mixing between cogenetic magmas involved in the generation of Zhangzhou calc-alkaline granite and show the advantage of using apatite geochemistry to track the magmatic evolution of granitoid batholiths.

Geological background

The geology of South China consists of Yangtze block in the northwest and Cathaysia block in the southeast, which were amalgamated in the Neoproterozoic along the Jiangnan Orogenic Belt (Fig. 1; Zhang et al. 2013). It underwent extensive tectonic and magmatic activity associated with the subduction of the paleo-Pacific Ocean during Mesozoic (Zhou et al. 2006). The distribution of Mesozoic igneous rocks in SE China is mainly controlled by several large-scale NE-trending faults such as the Zhenghe-Dafu and Changle-Nan'ao faults. The magmatism consists of predominant felsic lavas with minor intrusive mafic rocks (Zhou et al. 2006; Xu et al. 2020). Granitic rocks exposed in this region are mainly shallow-level, calc-alkaline, I-type granitoids that range from granodiorite, monzogranite to alkali-feldspar granite (Zhou et al. 2006; Li et al. 2014). These rocks also show hybrid geochemical signatures reflecting crust-mantle interaction that are typically observed at subduction zones (e.g., Griffin et al. 2002; Zhou et al. 2006; Guo et al. 2012; Xu et al. 2020). The contemporaneous mafic intrusive rocks are mainly hornblende gabbros, which show geochemical features similar to mafic arc cumulates (e.g., Li et al. 2014; Zhang et al. 2019).

The Zhangzhou batholith is located in the coastal region of Fujian province, SE China. Previous studies showed emplacement ages of this batholith ranging from 97 to 107 Ma (Chen et al. 2013). The calc-alkaline granite occurs as the main body of the batholith, consisting of granodiorite and monzogranite. In the field, abundant mafic microgranular enclaves (MMEs) occur in the monzogranite and both show a sharp contact relationship (Figs. 2a and 2b). The granodiorite is equigranular and consists of plagioclase (~45 vol%), K-feldspar (~25 vol%), quartz (~20 vol%), and biotite (5–8 vol%), with accessory zircon, apatite, titanite, allanite, and epidote. The major minerals in the monzogranite are K-feldspar (~35 vol%), quartz (~30 vol%), plagioclase (~25 vol%), and biotite (~5 vol%), with accessory zircon, apatite, allanite, and Fe-Ti oxides. The MMEs consist of plagioclase, biotite, and quartz, with or without K-feldspar, and accessory minerals include apatite, zircon, titanite, allanite, and Fe-Ti oxides (Chen et al. 2013). In the granite, apatite occurs as euhedral inclusions hosted in biotite, plagioclase, and titanite (Figs. 2c–2f). Based on field observations and geochemical studies, Chen et al. (2013) proposed that the calc-alkaline granite in the Zhangzhou batholith was formed by mixing between mantle- and crust-derived magmas.

Analytical methods

Whole-rock geochemical analyses

Whole-rock major oxides were determined by wavelength X-ray fluorescence spectrometry (XRF) at the Sample Solution Analytical Technology Co., Ltd., Wuhan, China. About 0.5 g of powder was thoroughly mixed with 3.6 g $Li_2B_4O_7$, 0.4 g LiF, 0.3 g NH_4NO_3, and minor LiBr in a platinum crucible. It was then melted in a furnace to form a glass disk for major element analysis. Trace element concentrations of the samples were determined by a Perkin-Elmer ELAN 6000 inductively coupled plasma-mass spectrometry (ICP-MS) after acid digestion in high-pressure polytetrafluoroethylene vessels at Guangzhou Institute of Geochemistry (GIG), Chinese Academy of Sciences (CAS). This involved mixing ~50 mg sample powder with 1 mL HF and 0.5 mL HNO_3 in a polytetrafluoroethylene beaker. Then the beaker was sealed in a stainless-steel vessel and heated at 190 °C for 48 h. The detailed analytical procedure was reported by Liu (1996). The analytical errors were 5% for rare earth element (REE) and high field strength element (HFSE), and 5 to ~10% for the other elements, based on repetitive analyses of USGS standards GSR-1 (granite), GSR-2 (andesite), and GSR-3 (basalt).

Whole-rock Sr and Nd isotope analyses were performed with a Finnigan Neptune multi-collector ICP-MS at the GIG-CAS, following the analytical procedures described by Li et al. (2006). The REE and Sr were separated via cation columns, and Nd fractions were further separated by HDEHP-coated Kef columns. The procedural blanks were <200 picogram (pg) for Sr and about 30 pg for Nd. The measured $^{87}Sr/^{86}Sr$ and $^{143}Nd/^{144}Nd$ ratios were normalized to $^{86}Sr/^{88}Sr = 0.1194$ and $^{146}Nd/^{144}Nd = 0.7219$, respectively. The reported $^{87}Sr/^{86}Sr$ and $^{143}Nd/^{144}Nd$ ratios were adjusted to the NBS SRM 987 standard ($^{87}Sr/^{86}Sr = 0.710247 \pm 8$, 2σ) and the JNdi-1 standard ($^{143}Nd/^{144}Nd = 0.512115 \pm 4$, 2σ, n = 4), respectively. Repeated analyses of NBS SRM 987 standard and the Shin Etsu JNdi-1 standard separately yielded mean values of 0.710247 ± 9 and 0.512115 ± 6 (2σ, n = 3). During whole-rock Sr-Nd isotope analyses, the USGS reference BHVO-2 (basalt) yielded $^{87}Sr/^{86}Sr = 0.703475 \pm 8$ (2σ, n = 6), $^{143}Nd/^{144}Nd = 0.512981 \pm 5$ (2σ, n = 6), consistent with the recommended values reported in Weis et al. (2005).

Electron microprobe (EMP) analysis

Backscattered electron (BSE) and cathodoluminescence (CL) images were performed with a SUPRA 55 SAPPHIRE equipped with a secondary electron and energy-dispersive X-ray spectrometry (EDS) detector. The concentrations of major elements in apatite, titanite, and plagioclase were determined by a Cameca SX FiveFe
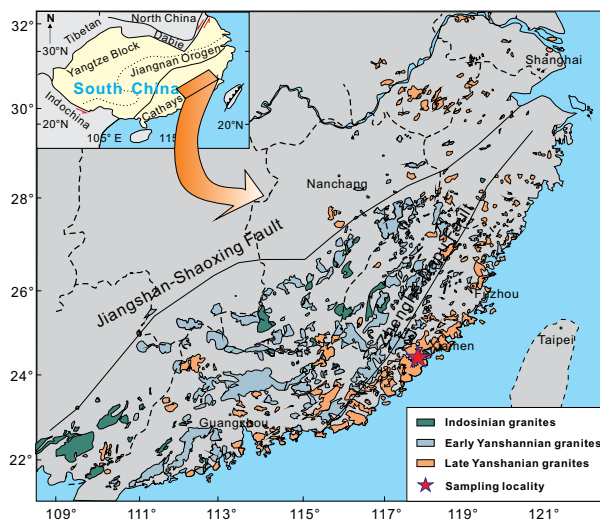
Figure 1. Simplified geological maps showing tectonic setting (after Zhang et al. 2013), and the distribution of Mesozoic granites in the coastal region of SE China (after Zhou et al. 2006). (Color online.)
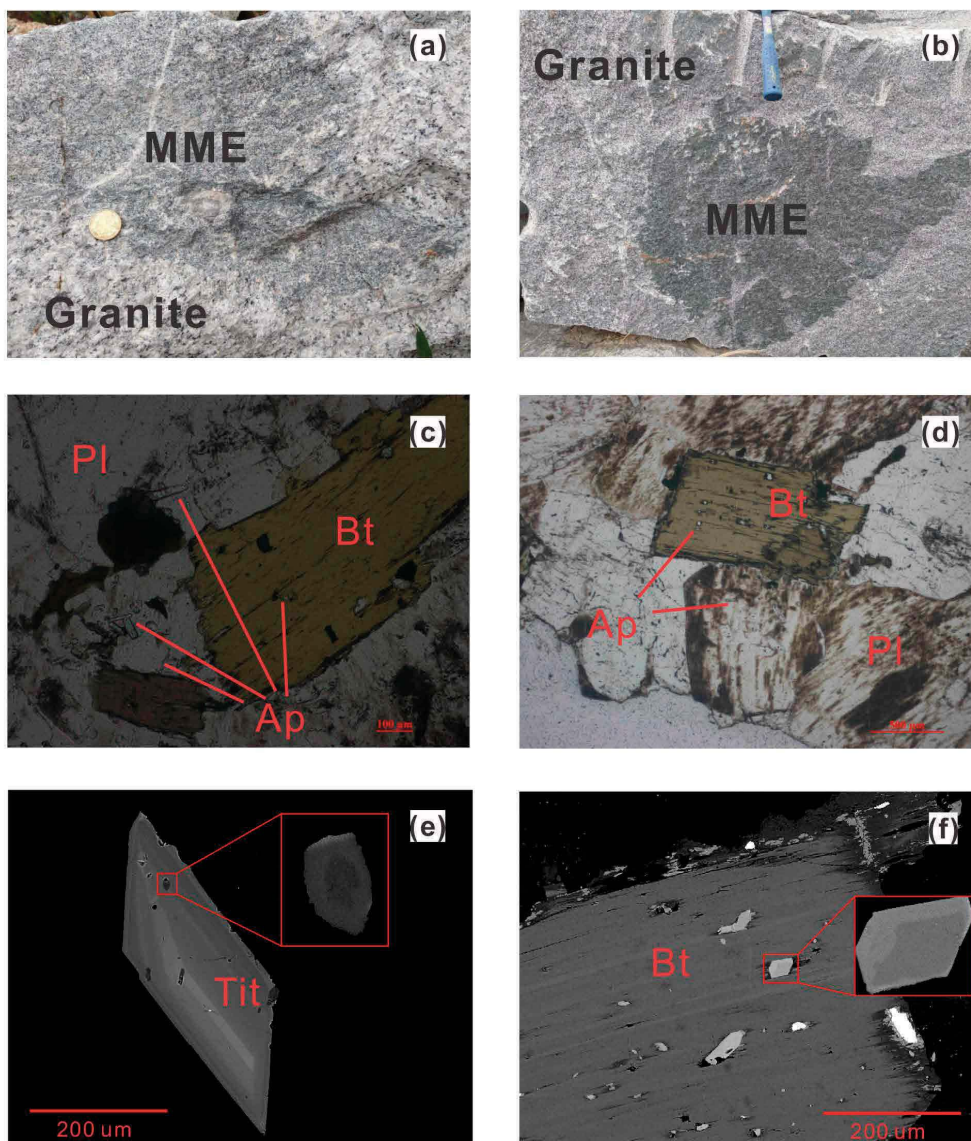
FIGURE 2. (a–b) Field photos showing the contact relationship between the host granite (monzogranite) and mafic microgranular enclaves. **(c–d)** Columnar apatite inclusions occurring in biotite and plagioclase. **(e–f)** BSE images showing zoned apatite hosted in titanite and biotite. (Color online.)

electron microprobe and JOEL JXA-8100 electron microprobe at the GIG-CAS. The operating conditions were 15 kV accelerating voltage, 20 nA probe current, and 5 μm spot diameter. The standards for adjustment include apatite for Ca and P; fluorite for F; sodalite for Cl; albite for Na; sanidine for K, Si, and Al; pyroxene for Mn, Fe, and Mg; and rutile for Ti, respectively. The analytical errors were within 1%.

LA-ICP-MS trace element analysis

Trace-element analyses of apatite, titanite, and zircon were performed with a Resolution M-50 laser ablation (LA) system coupled to an Agilent 7900a type inductively coupled plasma-mass spectrometer (ICP-MS) at the GIG-CAS. The detailed analytical procedure was reported in Tu et al. (2011). The diameter of the laser beam was 31 μm for zircon, apatite, and titanite (with 80 mJ laser energy, 6 Hz ablation frequency). Helium gas carrying the ablated sample aerosol is mixed with argon carrier gas prior to introduction into the ICP-MS. Each analysis included ~20 s of background acquisition (from a gas blank) followed by 45 s of data acquisition. ^{43}Ca was used as the internal standard for apatite and titanite, and ^{29}Si was used as the internal standard for zircon. The content of CaO in apatite and titanite was measured by EMPA and SiO_2 in zircon was assumed to be stoichiometric in zircon

with a concentration of ca. 32.8 wt%. NIST SRM 610 and 612 were employed as external standards, respectively, which were analyzed twice after every eight sample analyses. Data reduction was performed offline by the ICPMSDataCall software (Liu et al. 2008). The corresponding mean element concentrations of standards during this study are listed after the trace element concentrations for apatite, zircon, and titanite, respectively.

In situ Sr isotopic analysis of plagioclase

All in situ Sr isotope analyses in this study were performed on a Neptune Plus MC-ICP-MS (Thermo-Scientific), coupled with a RESOlution M-50 193 nm laser ablation system (Resonetics) at the GIG-CAS. The laser parameters were set as follows: beam diameter, 112–155 μm; repetition rate, 6 Hz; energy density, ~4 J cm^{-2}. Each analysis consisted of 250 cycles with an integration time of 0.262 s per cycle. During the first 30 s, the gas blank of the system was monitored with the laser beam off. In the following 30 s, the signals of ablated plagioclase were collected with the laser beam on. The gas blank of ^{83}Kr and ^{88}Sr was <2.5 mv and 0.5 mv, respectively, during the measurement of this study. The interferences of ^{84}Kr and ^{86}Kr on ^{84}Sr and ^{86}Sr were corrected by subtracting gas blank from the raw time-

resolved signal intensities. The mass bias of $^{87}Sr/^{86}Sr$ was normalized to $^{86}Sr/^{88}Sr =$ 0.1194 with an exponential law. The detailed data reduction procedure is reported in Zhang et al. (2015). Repeated analyses of the external standard NKT-1G yielded a weighted $^{87}Sr/^{86}Sr$ value of 0.70355 ± 0.00003 (2SD, n = 7), which is consistent with the reference value (0.70351 ± 0.00002, Elburg et al. 2005). The corresponding standard data during this study are listed after the Sr isotope of plagioclase.

In situ O isotope analyses of apatite and zircon

In situ oxygen isotope compositions of apatite were obtained using the Cameca IMS-1280 SIMS at the Institute of Geology and Geophysics, CAS. Separated apatite grains were embedded in epoxy disks together with apatite standards (Qinghu and Durango apatite). The Cs^+ primary ion beam was accelerated at 10 kV, with an intensity of ~2 nA, with spot sizes of about 20 μm in diameter. The normal-incidence electron flood gun was used to compensate for the charge at the surface of the gold-coated samples. Oxygen isotopes were measured using multi-collection mode on two off-axis Faraday cups. The analytical procedures of apatite were similar to those used for zircon oxygen isotopes as described by Li et al. (2010). In situ oxygen isotopes of zircon were also obtained using the Cameca IMS-1280 HR SIMS at the GIG-CAS. The analytical procedures of zircon are described by Xia et al. (2019). Measured $^{18}O/^{16}O$ ratios were normalized by using Vienna Standard Mean Ocean Water and compositions (V_{VSMOW}, $^{18}O/^{16}O = 0.0020052$), reported in standard per mil notation, and corrected for the instrumental mass fractionation factor (IMF). The IMF was obtained using the Durango fluorapatite and Penglai zircon as references for apatite and zircon, respectively. The average value of measured $\delta^{18}O$ of Durango apatites was 10.15‰ (2SD = 0.56, n = 26), which is similar to the result in Trotter et al. (2008). The Qinghu apatite was also analyzed as an external reference for apatite, with a $\delta^{18}O$ value of 5.59‰ (2SD = 0.52, n = 31). The $\delta^{18}O$ values of the Durango and Qinghu apatite and Penglai and Qinghu zircon are listed after the $\delta^{18}O$ values for apatite and zircon, respectively.

RESULTS

Whole-rock geochemistry

Whole-rock compositions are listed in Online Material[1] Table OM1. The rocks of the Zhangzhou batholith show large variations in SiO_2 contents. The gabbro and diorite together have SiO_2 ranging from 49.9 to 60.1 wt% with relatively high Mg-number (Mg# = 48 to 52). The calc-alkaline granites (monzogranites and granodiorites) span a SiO_2 range from 63.0 to 71.0 wt%, with an Mg-number ranging from 34 to 43. The granites are metaluminous with A/CNK between 0.92 and 0.99. Monzogranites (Sample No. 17ZZ05 and 17ZZ06) generally contain higher SiO_2 content than the granodiorites (67.8–71.0 vs. 63.0–66.8 wt%), ΣREE (212–309 vs. 135–235 ppm), and K_2O (3.59–4.51 vs. 2.83–3.50 wt%), but lower CaO (2.22 to 2.87 vs. 3.86–4.79 wt%) and MgO (0.79–1.12 vs. 1.33–2.07 wt%). In contrast, the alkali feldspar granite has the highest SiO_2 content with a range from 76.4 to 77.6 wt% and the lowest Mg-number (Mg# = 16 to 22). All rock types have similar initial $^{87}Sr/^{86}Sr$ ratios, ranging from 0.70602 to 0.70742. The mafic rocks have $\varepsilon_{Nd}(t)$ values ranging from –2.7 to –2.8, while the felsic rocks have slightly lower $\varepsilon_{Nd}(t)$ values between –3.2 and –4.2 (Online Material[1] Table OM1). Thus, the mafic and felsic rocks together form an igneous complex with almost similar isotope compositions.

Texture and geochemistry of apatite

Representative BSE images for apatite from the calc-alkaline granite are presented in Figure 3. These apatite grains are mostly prismatic, with sizes ranging from 100 to 200 μm (Figs. 2c–2f and 3). They commonly occur as inclusions hosted in the major mineral phases (Figs. 2c–2f), indicating apatite was an early crystallizing phase. Most of the apatite grains exhibit a core-rim zonation texture with a dark core and bright rims in the BSE images (Fig. 3). The dark core spans a range of 30–100 μm in size, and the bright rims range from 20 to 40 μm in width (Fig. 3).

The compositions of the analyzed apatite are listed in Online Material[1] Table OM2. Both the apatite core and rim domains are fluorapatite with F > 2.5 wt% and F/Cl ratio >11.5 (Figs. 4a and 4b). They show similar P_2O_5 (41.1–43.3 wt%), CaO (53.4–57.9 wt%), FeO (0.01–0.12 wt%), and MnO (0.16–0.29 wt%). However, the apatite core domains generally contain higher SO_3 (0.28–1.00 vs. 0.10–0.42 wt%), Na_2O (0.08–0.30 vs. 0.02–0.11 wt%), and lower SiO_2 (0.01–0.20 vs. 0.26–0.58 wt%) contents
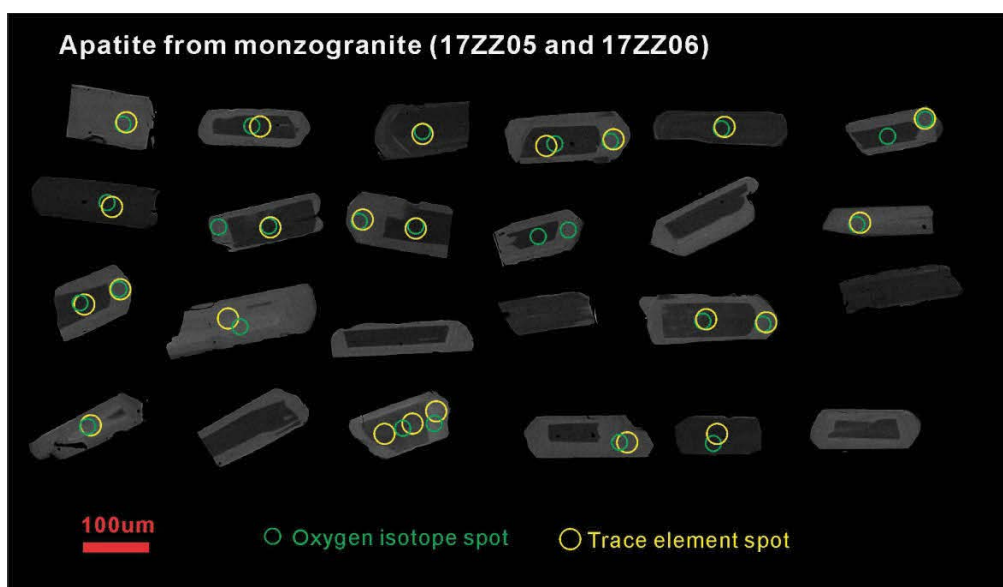
FIGURE 3. Representative BSE images of apatite from the Zhangzhou calc-alkaline granite. Most crystals show a core-rim zonation texture. (Color online.)
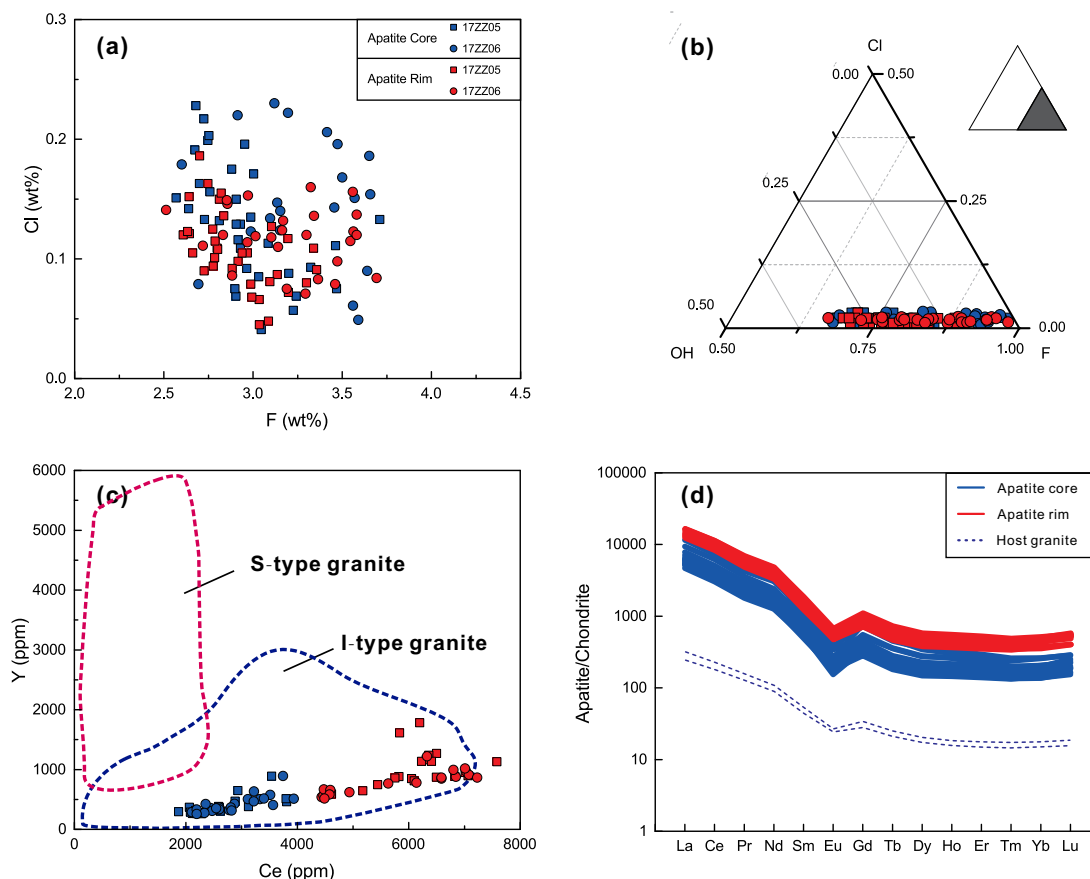
Figure 4. Plots of Cl vs. F (**a**), Cl-OH-F (**b**), Y vs. Ce (ppm) (**c**) of apatite, and chondrite-normalized REE patterns of apatite (**d**). In **b**, the concentrations of volatile components (atomic proportions) in apatite is estimated by using the method by Piccoli and Candela (2002). In **c**, the variation fields of apatite in S-type and I-type granite are from Laurent et al. (2017). Normalization values (**d**) are from McDonough and Sun (1995). (Color online.)

than the rim domains. Also, the core domains generally have higher Li concentrations (2.0 to 19.2 vs. 0.6 to 4.3 ppm) but lower REE (ΣREE = 3989 to 9743 vs. 9380 to 16 417 ppm) and Y (Y = 259 to 894 vs. 517 to 1781 ppm) concentrations than the rim domains. Nevertheless, all apatite domains have relatively high Ce/Y ratios, within the compositional fields of apatite from "I-type granitoids" (Fig. 4c; Laurent et al. 2017), and show right-declined chondrite-normalized REE patterns with similar Ce/Ce* and Eu/Eu* ratios (Fig. 4d). Major and trace element analyses from a profile across a representative zoned apatite grain show abrupt compositional variations (Fig. 5; Online Material[1] Table OM2). From core to rim, the SO_3 concentration decreases from 0.73 to 0.16 wt% and Cl decreases from 0.11 to 0.05 wt%, whereas SiO_2 increases from 0.27 to 0.70 wt% (Figs. 5b–5d). The apatite rims have 6587 to 7009 ppm Ce and 866 to 1017 ppm Y, up to three times the concentrations in the core domain (Ce = 2354 to 2874 ppm, Y = 338 to 428 ppm; Figs. 5f and 5g). The apatite rims also have higher Sr (Sr = 223 to 230 vs. 135 to 166 ppm; Fig. 5h). In contrast, the apatite cores contain 5.1–7.4 ppm Li and 0.11–0.18 wt% Na_2O, much higher than those in the rims (Li = 1.3–3.0 ppm, Na_2O = 0.03–0.04 wt%; Figs. 5e and 5i).

The O isotope compositions of apatite are listed in Online Material[1] Table OM2 and plotted in Figure 6. Both the apatite core and rim domains have mantle-like O isotopic compositions regardless of their difference in ΣREE (Fig. 6). The core domains have $\delta^{18}O$ values ranging from 5.3‰ (2SE = 0.28) to 6.8‰ (2SE = 0.26) with an average of 6.0‰ (n = 21), and the apatite rim domains have $\delta^{18}O$ values ranging from 5.2‰ (2SE = 0.32) to 6.4‰ (2SE = 0.37) with an average of 5.8‰ (n = 21).

Textures and geochemistry of other minerals

Zircon. The compositions of zircon are listed in Online Material[1] Table OM3. Zircon is hosted in main mineral phases such as plagioclase and biotite. It exhibits a euhedral prismatic form, ranges from 50 to 200 μm in diameter with length/width ratios from 2:1 to 3:1, and typical igneous oscillatory zoning in CL images (Online Material[1] Fig. OM1). The Hf concentration of zircon ranges from 7695 to 11 489 ppm, is negatively correlated with the concentrations of Ti (3.1 to 16.7 ppm) and P (332 to 696 ppm) and with Th/U (0.54 to 1.48) and Eu/Eu* (0.4 to 1.2), but is positively correlated with Yb/Gd (7.9 to 27.8). The Ti-in-zircon (T_{Ti-Zr}) thermometer yields values ranging from 674 to 835 °C (Online Material[1] Table OM3) using the equations of Ferry and Watson (2007). Zircon also has mantle-like $\delta^{18}O$
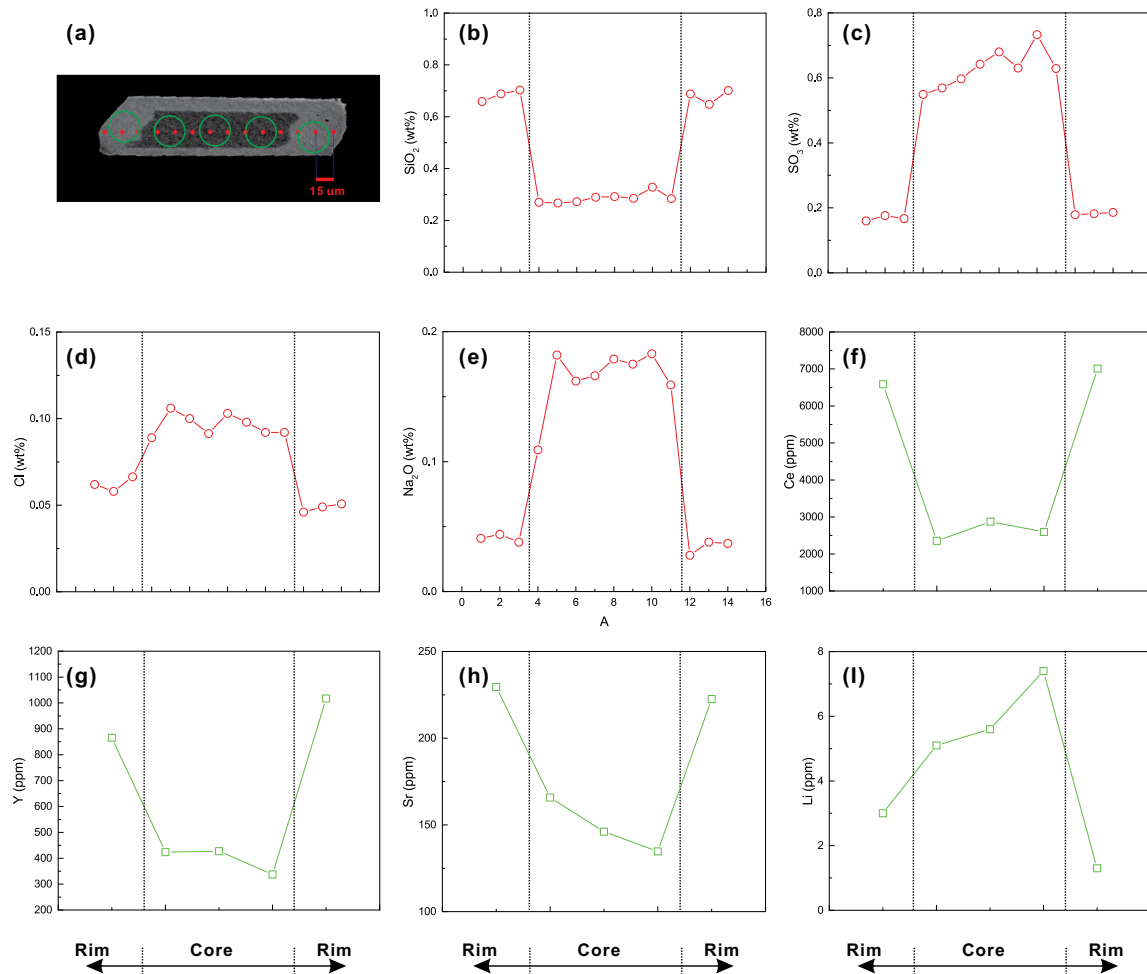
Figure 5. Core-to-rim profiles of major and trace element compositions of a zoned apatite crystal from the Zhangzhou calc-alkaline granite. (**a**) The BSE image showing the core-to-rim analyzed profiles. (**b**–**e**) EPMA analysis, variations in SiO_2 (**b**), SO_3 (**c**), Cl (**d**), and Na_2O (**e**) across the profile. (**f**–**i**) LA-ICPMS analysis, variations in Ce (**f**), Y (**g**), Sr (**h**), and Li (**i**) across the profile. (Color online.)

values ranging from 5.3 to 6.9‰ with an average of 5.8‰ (SD = 0.44, n = 20).

Titanite. The compositions of titanite are listed in Online Material[1] Table OM4. Titanite crystals always display continuous and oscillatory zoning in BSE images, showing small intracrystalline compositional changes. Some titanite crystals show an obvious zoned texture with a bright core and dark rim. The bright core often shows fir-tree and oscillatory zonation. The dark rim shows a uniform texture and is occasionally surrounded by bright domains (Online Material[1] Fig. OM2). Titanite frequently contains inclusions of the zoned apatite (Fig. 2e). Titanite from the granites has weakly variable SiO_2 (29.02–30.74 wt%), TiO_2 (34.04–36.81wt%), CaO (26.37–29.33 wt%), Al_2O_3 (1.02–1.65 wt%), FeO (1.48–2.49 wt%), and F (0.05–0.42 wt%). However, the total REE concentrations of titanite varies greatly from 1.7 to 2.9 wt%. The bright domains generally have much higher REE concentrations than the dark parts.

Plagioclase. The compositions of plagioclase are listed in Online Material[1] Table OM5. Plagioclase crystals in the granite show complex textures and zoning patterns. Some grains have a strong dissolution texture, with sodic patches in the dissolved calcic cores and less calcic rims (Online Material[1] Fig. OM3). The dissolved core has a sieved texture and higher Ca contents (An_{38}–An_{48}), whereas the dark patches in the core and the rim have lower Ca contents (An_{14}–An_{30}). Such a compositional zonation might be caused during decompression of the magma. Twelve analytical spots on plagioclase from the granite show a narrow variation of initial $^{87}Sr/^{86}Sr$ ratios from 0.7064 to 0.7067 with an average of 0.7066 (n = 12). This value is quite similar to the host bulk rock [$^{87}Sr/^{86}Sr_{(i)}$ = 0.7066].

Discussion

Core-rim zonation texture in apatite: A record of magma mixing

The apatite in Zhangzhou granite is characterized by textural and compositional zonation with abrupt core to rim increases in SiO_2 and REE concentrations and decreases in SO_3 and Li (Figs. 3 and 5). Compositional zoning of minerals in igneous rocks results from various processes, including fractional crystallization, AFC processes, post-crystallization hydrothermal activity, and
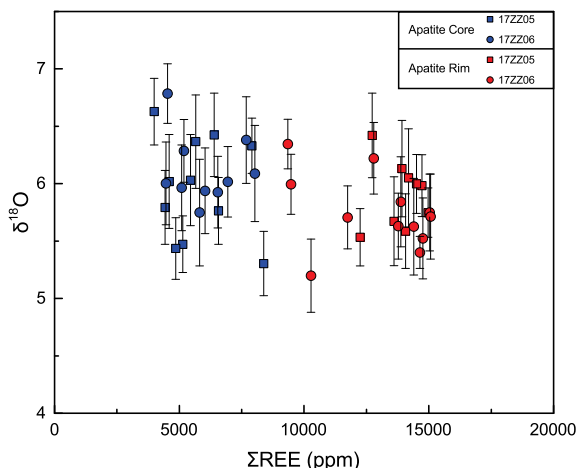
FIGURE 6. Plot of ΣREE (ppm) vs. $\delta^{18}O$, the bars denote the analytical errors given as 2σ. (Color online.)

FIGURE 7. Plots of SiO_2 (wt%) vs. SO_3 (wt%). (Color online.)

magma mixing. In the following, we discuss the possible effects of these processes on the compositional variations observed in the apatite from Zhangzhou granite.

(1) Fractional crystallization plays an important role in progressive mass and ionic exchange between magma and minerals. Compositional zonation in the crystallizing phase typically follows "normal" igneous trends (i.e., increases in incompatible elements and decreases in compatible elements from core to rims, Gao et al. 2007; Guo et al. 2007; Streck 2008). Since REEs behave as incompatible elements in plagioclase, biotite, and quartz (Nash and Crecraft 1985)—the major mineral assemblage in the Zhangzhou granite, fractionation of these minerals would lead to increasing REE concentrations in the crystallizing apatite. Biotite-dominated fractionation may also cause halogen variation in a crystallizing magma and possibly results in Cl/F zonation in apatite (Teiber et al. 2014; Ansberque et al. 2019). Fractionation of biotite + plagioclase + quartz might explain the core to rim increases in REE concentrations and decreasing Cl/F in zoned apatite from the Zhangzhou granite, but it cannot explain the observed rim to core trends to higher SiO_2 and Sr concentrations (Figs. 5b and 5h) and similar Fe concentrations. Fractional crystallization of significant amounts of apatite might explain progressive core to rim decreases in REE concentrations in zoned apatite (e.g., Bruand et al. 2014) because REEs are compatible in apatite (e.g., Prowatke and Klemme 2006). However, such trends contrast with the abrupt increase in concentration from the core to rim that we observe (Figs. 5f and 5g). In any case, fractional crystallization is a continuous process that likely forms continuous compositional zonations or predictable changes reflected in changing modal mineral assemblages, e.g., a progressive increase of La in clinopyroxene from core to rim during fractional crystallization (Gao et al. 2007). Therefore, it is clear that the sharp core to rim compositional variations in apatite of the Zhangzhou granite could not be generated by fractional crystallization alone (Figs. 5 and 7).

(2) Similar to fractional crystallization, AFC processes also generally result in the crystallization of minerals with normal compositional zonation (e.g., Jung et al. 1999). However, in
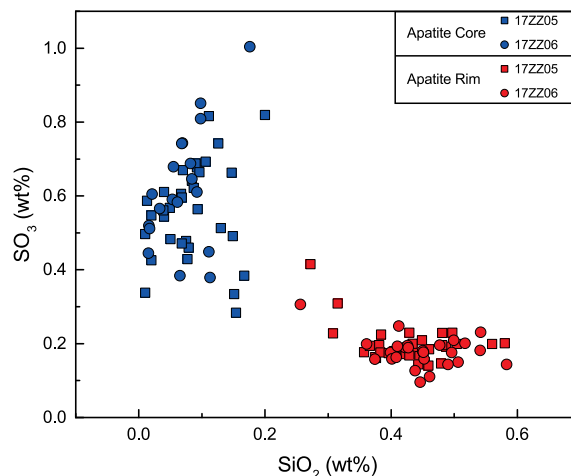
the Zhangzhou granite, there are weak correlations between the $^{87}Sr/^{86}Sr_{(i)}$ and $\varepsilon_{Nd}(t)$ and SiO_2 [SiO_2 = 67.8–71.0 wt%, $^{87}Sr/^{86}Sr_{(i)}$ = 0.7062–0.7066, and $\varepsilon_{Nd}(t)$ = –3.0 to –4.2; Online Material[1] Table OM1]. The plagioclase in these granites, with variable An contents, has a uniform Sr isotope composition (An = 16–48, $^{87}Sr/^{86}Sr_{(i)}$ = 0.7064–0.7067; Online Material[1] Table OM5), similar to the whole rock value [$^{87}Sr/^{86}Sr_{(i)}$ = 0.7066]. Apatite core and rim domains, as well as zircon, have similar oxygen isotope compositions (Online Material[1] Table OM3). All these geochemical features do not support a significant role in crustal contamination or assimilation.

(3) Hydrothermal fluids have been shown to leach REE from apatite, resulting in substantial decreases in REE concentrations and variations in LREE/HREE ratios as well as O isotopes in apatite with the formation of new REE-phosphates such as monazite and xenotime (e.g., Rae et al. 1996; Harlov and Förster 2003; Harlov et al. 2005; Broom-Fendley et al. 2016; Zeng et al. 2016; Birski et al. 2019). While apatite crystals in the Zhangzhou granite have REE-poor cores, it is unlikely that this compositional zonation resulted from post-crystallization hydrothermal activity because the apatite core domains have La/Sm ratio and $\delta^{18}O$ value similar to the rim domains (Figs. 4d and 6), and co-existing secondary mineral phases are absent (Figs. 2c–2f and 3).

(4) Magma mixing can produce textural and compositional zoning in apatite (Tepper and Kuehner 1999; Słaby et al. 2012; Bruand et al. 2014; Laurent et al. 2017), accounting for sharp compositional variations like those observed in apatite from the Zhangzhou granite. Experimental results have shown nonlinear element exchange between the interacting magmas due to variations in diffusion behavior (De Campos et al. 2008; Perugini et al. 2008). The direction of compositional change in mineral compositions is largely a reflection of the new bulk magma composition after each mixing step and might reverse trends expected from fractional crystallization (with or without crustal contamination) alone. In the case of the Zhangzhou granite, magma mixing is strongly supported by the presence of MMEs and granodiorite inclusions in the monzogranite at the locality from which the samples were taken (Figs. 2a and 2b). Mixing is also reflected in abrupt ΣREE variations in the zoned titanite (Online Material[1]). Thus, magma mixing is our preferred model

in explaining the composition zonations that we see in apatite from the Zhangzhou granite.

Composition of end-member melts during magma mixing

The rapid core-to-rim increases in SiO_2, REE, and Y concentrations and decreases in SO_3 and Li of apatite from the Zhangzhou granite can probably be attributed to abrupt changes in bulk melt composition and/or the resultant change in partition coefficients during the apatite crystallization (Fig. 5). For simplicity, we assume a single mixing event and name the magma that crystallized the apatite cores as Batch I and the mixed magma that crystallized the apatite rims as Batch II.

Previous studies have demonstrated that the REE contents in apatite are primarily controlled by magma composition and mineral/melt partition coefficients (D) (Sha and Chappell 1999; Prowatke and Klemme 2006). Increasing SiO_2 content in a fractionating melt is expected to promote the coupled substitution reaction: $REE^{3+} + SiO_4^{4-} = Ca^{2+} + PO_4^{3-}$ (Pan and Fleet 2002), and to further increase the degree to which REE preferentially partition into apatite rather than melt (i.e., increasing $D_{REE}^{Ap/melt}$) (Prowatke and Klemme 2006). Experimental results have also shown that $D_{REE}^{Ap/melt}$ values depend largely on the composition of magma, showing a strong positive correlation with silica content of magma (e.g., Watson and Green 1981; Prowatke and Klemme 2006; Laurent et al. 2017). This is consistent with the previous investigations on apatite from a wide range of magmatic suites, which found that REE concentrations in apatite increase from the primitive to evolved rocks (Sha and Chappell 1999; Belousova et al. 2002; Chu et al. 2009; Zhang et al. 2020). Therefore, apatite crystallized from a high-SiO_2 magma tends to contain high SiO_2 and REE concentrations (Ladenburger et al. 2016). Given that the ΣREE and SiO_2 concentration of apatite rims can be three times higher than cores (Figs. 5b, 5f, and 5g), we suggest that the SiO_2 content of Batch II magma was relatively high, with a correspondingly high-$D_{REE}^{Ap/melt}$.

Theoretically, sulfur concentration in apatite depends largely on the S content of the melt, and it can be used as a proxy to track the sulfur evolution of magma (Parat et al. 2002, 2011; Van Hoose et al. 2013; Brounce et al. 2019). The partition coefficient of sulfur in apatite ($D_S^{Ap/melt}$) is additionally controlled by complex physio-chemical conditions, including oxygen fugacity (f_{O_2}) and temperature (Peng et al. 1997; Parat and Holtz 2004). Both apatite core and rim domains show similar Eu/Eu* and Ce/Ce* (Fig. 4d), probably suggesting crystallization under similar oxidizing conditions (e.g., Sha and Chappell 1999; Cao et al. 2012). On the other hand, because the apatite cores and rims occur in the same samples, the similar apatite saturation temperature should have little effect on $D_S^{Ap/melt}$. Therefore, the high S content in apatite cores, which can be four times higher than the apatite rims, is likely attributed to higher sulfur concentration in Batch I magma (Figs. 5c and 7).

Constraints on the magma source

Both core and rim domains in apatite from the Zhangzhou granite exhibit mantle-like $\delta^{18}O$ values in equilibrium with the coeval zircon (Fig. 6; Online Material[1] Table OM3). The granites have whole-rock $^{87}Sr/^{86}Sr_{(i)}$ and $\varepsilon_{Nd}(t)$ values similar to those of MMEs and mafic rocks in the Zhangzhou batholith (Chen et al. 2013). These geochemical features suggest the derivation of the Zhangzhou granite from newly accreted crust.

As mentioned early, the core and rim domains in apatite from the Zhangzhou granite have distinct chemical compositions, especially the high-SO_3 content (up to 1.00%) in the core domain. Apatite incorporates sulfur in multiple oxidation states (i.e., S^{6+}, S^{4+}, and S^{2-}) via complex substitutions (Piccoli and Candela 2002; Konecke et al. 2017; Brounce et al. 2019). However, previous studies have shown that apatite favors coupled substitution mechanisms involving oxidized S (Streck and Dilles 1998; Kim et al. 2017), and S-rich apatite always crystallizes at a high oxygen fugacity (e.g., Parat et al. 2011; Chelle-Michou and Chiaradia 2017). This is consistent with the oxidized nature of the I-type, or magnetite-series, Zhangzhou granite (e.g., Ishlhara 1977; Carmichael 1991; Blevin and Chappell 1995).

At subduction zones, seawater sulfate can be absorbed by the sediments overlying the mafic oceanic crust during seafloor hydrothermal alteration. During subduction of the oceanic crust and overlying sulfate-bearing sediments, oxidized sulfur is released into the mantle wedge (e.g., Sasaki and Ishihara 1979; de Hoog et al. 2001; Wallace and Edmonds 2011). Arc mafic magmas derived from the mantle wedge metasomatized by sulfate-bearing sediments should correspondingly contain high S (e.g., Sharma et al. 2004), consistent with previous experiments that oxidized arc mafic magmas have a high capacity to contain sulfur (Jugo et al. 2005). For instance, olivine-hosted melt inclusions from the arc mafic magmas can contain high S content up to 7000 ppm (Wallace and Edmonds 2011). An oxidized mafic melt can transport large amounts of sulfur from the mantle to shallow crustal levels and even to the atmosphere (e.g., de Hoog et al. 2004; Richards 2015; Zellmer et al. 2015). Underplated mafic magmas might be the source of high-S arc crust formed during the subduction of paleo-Pacific Ocean in the Cretaceous. Previous studies have also suggested that mafic intrusions might supply sulfur to long-lived felsic magma chambers (Edmonds et al. 2010; Wallace and Edmonds 2011), in which high-S apatite crystallizes (Van Hoose et al. 2013). Thus, underplated mafic magmas releasing S-rich fluid and/or resultant melting of the high-S arc crust could have been the source of the high-S felsic Batch I magma that crystallizes the cores of apatite in the Zhangzhou granite.

Devolatilization of Batch II magma

Liquid-vapor fractionation is considered to be an important process of magmatic differentiation where a separate vapor phase co-exists with magma (Webster and Vivo 2002; Baker and Alletti 2012). This process can cause geochemical variations related to the difference in element partitioning between the co-existing vapor and magma. In the case of the Zhangzhou granite, liquid-vapor fractionation probably contributes to the large variations in concentrations of fluid-mobile elements such as S, Cl, and Li in the apatite.

As discussed above, Batch II magma had higher SiO_2 but lower S than Batch I magma. Considering the evidence, based on tightly constrained isotopic variations, that both magma batches shared a common source, there must have been an additional geological process that rapidly decreased the S content during the evolution of Batch II magma. Possible mechanisms to reduce the S content of magma include (1) fractionation of sulfide and sulfate (e.g., anhydrite and pyrite); and (2) devolatilization (evap-

oration of magmatic H_2S and/or SO_2-rich fluid exsolution). Since anhydrite and pyrite are not observed in the studied samples, it seems unlikely that the granitic magma was saturated in sulfide or sulfate minerals. Hence, the reduced S content is unlikely to be supplied by sulfate and sulfide fractionation. Therefore, SO_2 disproportionation in an exsolved fluid (e.g., Mavrogenes and Blundy 2017) and/or direct degassing as magmatic H_2S (e.g., Oppenheimer et al. 2011), might be realistic alternative means of lowering the S content in Batch II magma. The oxidation state of I-type granitic magma implies that the majority of S in the magma existed as SO_4^{2-} instead of H_2S (Baker and Moretti 2011; Richards 2015), suggesting a more important role of fluid exsolution than degassing of H_2S during magmatic evolution.

Since Cl preferentially partitions into fluids but F is soluble in melts (Baker and Alletti 2012; Webster et al. 2018), devolatilization can also lead to a decrease in Cl concentration of a melt, and in any crystallizing apatite, without significantly affecting F concentrations (e.g., Piccoli and Candela 2002; Webster 2004; Aiuppa et al. 2009; Balcone-Boissard et al. 2010; Zhang et al. 2012; Teiber et al. 2014; Wang et al. 2018). Apatite rims have lower Cl content and Cl/F than the core for any given zoned apatite, consistent with the effect of devolatilization (Fig. 5d; Online Material[1] Table OM2). The indistinguishable ranges in F and Cl concentrations of all apatites (Fig. 4a) are probably due to variable crystallization conditions (Boyce et al. 2014).

Devolatilization is also evidenced by the lower Li concentration in the apatite rims (Fig. 5i). Since Li preferentially enters aqueous fluid rather than the silicate melt, devolatilization would lead to a Li decrease in both the melt and crystallizing apatite (Webster et al. 1989; Duan and Jiang 2018). Collectively, Batch II magma experienced strong devolatilization, which is consistent with the previous observations that exsolved fluids have the capacity to sequester Li, Cl and S away from the magmatic systems (e.g., Bai and Koster van Groos 1999; Kamenetsky et al. 1999; Webster 2004; Zajacz et al. 2008; Pokrovski et al. 2013).

PETROGENETIC IMPLICATIONS

It is commonly assumed that elevated $\varepsilon_{Nd}(t)$ or $\varepsilon_{Hf}(t)$ values in granitoids implies mixing by mantle-derived magma, whereas more constant isotopic compositions in granite reflect the predominant role of fractional crystallization. For example, various degrees of mixing between mantle-derived mafic and crust-derived felsic magmas result in a wide $\varepsilon_{Hf}(t)$ range of the calc-alkaline felsic rocks in SE China (Griffin et al. 2002; Guo et al. 2012). However, in many magmatic systems and tectonic environments, interaction of cogenetic magmas is also inevitable as magma chambers are incrementally, or episodically, filled by magma batches from common sources over time (Taylor 2004; Annen 2009; Farina et al. 2012). In such cases, important magmatic processes such as crystal-melt segregation, liquid-vapor fractionation, and self-mixing in crustal magma chamber can be difficult to monitor by traditional bulk-rock geochemical analyses (Turner and Campbell 1986; Couch et al. 2001; Alves et al. 2009; Edmonds and Woods 2018; Sun et al. 2019; Yan et al. 2020). Mixing of cogenetic granitic magmas and devolatilization process, as shown here for the Zhangzhou granite, have occurred with little or no isotopic variation.

More recent studies on granite petrogenesis have benefited from advances in analytical techniques that enable in situ analysis of minerals for stable and radiogenic isotopes, including O, S, Rb-Sr, Sm-Nd, and Lu-Hf systems (e.g., Griffin et al. 2002; Yang et al. 2014; Economos et al. 2017; Bruand et al. 2019; Cao et al. 2019). Such studies have shown that in situ geochemical analysis on minerals (e.g., apatite, plagioclase, zircon, and titanite) has many advantages over whole-rock chemistry in petrogenetic discussion (e.g., Yu et al. 2018; Gros et al. 2020; Zhang et al. 2020). Apatite performs particularly well as a recorder of petrogenetic processes, and our study provides an example illustrating the advantages of using compositional zonations in apatite to track obscure magma processes such as mixing of cogenetic granitic magmas and devolatilization. There is no doubt that in situ compositional and isotopic analysis of apatite will provide significant advances in the range of data available for understanding igneous petrogenesis.

REFERENCES CITED

Aiuppa, A., Baker, D.R., and Webster, J.D. (2009) Halogens in volcanic systems. Chemical Geology, 263, 1–18.

Alves, A., de Assis Janasi, V., Simonetti, A., and Heaman, L. (2009) Microgranitic enclaves as products of self-mixing events: a study of open-system processes in the Maua granite, Sao Paulo, Brazil, based on in situ isotopic and trace elements in plagioclase. Journal of Petrology, 50, 2221–2247.

Annen, C. (2009) From plutons to magma chambers: Thermal constraints on the accumulation of eruptible silicic magma in the upper crust. Earth and Planetary Science Letters, 284, 409–416.

Ansberque, C., Mark, C., Caulfield, J.T., and Chew, D.M. (2019) Combined in-situ determination of halogen (F, Cl) content in igneous and detrital apatite by SEM-EDS and LA-Q-ICPMS: A potential new provenance tool. Chemical Geology, 524, 406–420.

Ayers, J.C., and Watson, E.B. (1993) Apatite/fluid partitioning of rare-earth elements and strontium: Experimental results at 1.0 GPa and 1000 °C and application to models of fluid-rock interaction. Chemical Geology, 110, 299–314.

Bai, T.B., and Koster van Groos, A.F. (1999) The distribution of Na, K, Rb, Sr, Al, Ge, Cu, W, Mo, La, and Ce between granitic melts and co-existing aqueous fluids. Geochimica et Cosmochimica Acta, 63, 1117–1131.

Baker, D.R., and Alletti, M. (2012) Fluid saturation and volatile partitioning between melts and hydrous fluids in crustal magmatic systems: The contribution of experimental measurements and solubility models. Earth-Science Reviews, 114, 298–324.

Baker, D.R., and Moretti, R. (2011) Modeling the solubility of sulfur in magmas: A 50-year old geochemical challenge. Reviews in Mineralogy and Geochemistry, 73, 167–213.

Balcone-Boissard, H., Villemant, B., and Boudon, G. (2010) Behaviour of halogens during the degassing of felsic magmas. Geochemistry, Geophysics, Geosystems, 11, Q09005. doi:10.1029/2010GC003028.

Belousova, E.A., Griffin, W.L., O'Reilly, S.Y., and Fisher, N.I. (2002) Apatite as an indicator mineral for mineral exploration: Trace-element compositions and their relationship to host rock type. Journal of Geochemical Exploration, 76, 45–69.

Birski, Ł., Słaby, E., Wirth, R., Koch-Müller, M., Simon, K., Wudarska, A., Götze, J., Lepland, A., Hofmann, A., and Kuras, A. (2019) Archaean phosphates: A case study of transformation processes in apatite from the Barberton greenstone belt. Contributions to Mineralogy and Petrology, 174, 25.

Blevin, P.L., and Chappell, B.W. (1995) Chemistry, origin, and evolution of mineralized granites in the Lachlan fold belt, Australia; the metallogeny of I- and S-type granites. Economic Geology, 90, 1604–1619.

Boyce, J.W., Tomlinson, S.M., McCubbin, F.M., Greenwood, J.P., and Treiman, A.H. (2014) The lunar apatite paradox. Science, 344, 400–402.

Broom-Fendley, S., Heaton, T., Wall, F., and Gunn, G. (2016) Tracing the fluid source of

heavy REE mineralisation in carbonatites using a novel method of oxygen-isotope analysis in apatite: The example of Songwe Hill, Malawi. Chemical Geology, 440, 275–287.

Brounce, M., Boyce, J., McCubbin, F.M., Humphreys, J., Reppart, J., Stolper, E., and Eiler, J. (2019) The oxidation state of sulfur in lunar apatite. American Mineralogist, 104, 307–312.

Bruand, E., Storey, C., and Fowler, M. (2014) Accessory mineral chemistry of high Ba-Sr granites from northern Scotland: Constraints on petrogenesis and records of whole-rock signature. Journal of Petrology, 55, 1619–1651.

Bruand, E., Fowler, M., Storey, C., and Darling, J. (2017) Apatite trace element and isotope applications to petrogenesis and provenance. American Mineralogist, 102, 75–84.

Bruand, E., Storey, C., Fowler, M., and Heilimo, E. (2019) Oxygen isotopes in titanite and apatite, and their potential for crustal evolution research. Geochimica et Cosmochimica Acta, 255, 144–162.

Cao, M., Li, G., Qin, K., Seitmuratova, E.Y., and Liu, Y. (2012) Major and trace element characteristics of apatites in granitoids from central Kazakhstan: Implications for petrogenesis and mineralization. Resource Geology, 62, 63–83.

Cao, M., Evans, N.J., Qin, K., Danišík, M., Li, G., and McInnes, B.I.A. (2019) Open apatite Sr isotopic system in low-temperature hydrous regimes. Journal of Geophysical Research: Solid Earth, 124, 11,192–11,203.

Carmichael, I.S.E. (1991) The redox states of basic and silicic magmas: a reflection of their source regions? Contributions to Mineralogy and Petrology, 106, 129–141.

Chappell, B.W., and White, A.J.R. (1974) Two contrasting granite types. Pacific Geology, 8(2), 173–174.

Chelle-Michou, C., and Chiaradia, M. (2017) Amphibole and apatite insights into the evolution and mass balance of Cl and S in magmas associated with porphyry copper deposits. Contributions to Mineralogy and Petrology, 172.

Chen, J.-Y., Yang, J.-H., Zhang, J.-H., Sun, J.-F., and Wilde, S.A. (2013) Petrogenesis of the Cretaceous Zhangzhou batholith in southeastern China: Zircon U-Pb age and Sr-Nd-Hf-O isotopic evidence. Lithos, 162-163, 140–156.

Cherniak, D.J. (2010) Diffusion in accessory minerals: Zircon, titanite, apatite, monazite and xenotime. Reviews in Mineralogy and Geochemistry, 72, 827–869.

Chu, M.F., Wang, K.L., Griffin, W.L., Chung, S.L., O'Reilly, S.Y., Pearson, N.J., and Iizuka, Y. (2009) Apatite composition: Tracing petrogenetic processes in Transhimalayan granitoids. Journal of Petrology, 50, 1829–1855.

Couch, S., Sparks, R.S.J., and Carroll, M.R. (2001) Mineral disequilibrium in lavas explained by convective self-mixing in open magma chambers. Nature, 411, 1037–1039.

De Campos, C.P., Dingwell, D.B., Perugini, D., Civetta, L., and Fehr, T.K. (2008) Heterogeneities in magma chambers: Insights from the behavior of major and minor elements during mixing experiments with natural alkaline melts. Chemical Geology, 256, 131–145.

de Hoog, J.C.M., Mason, P.R.D., and van Bergen, M.J. (2001) Sulfur and chalcophile elements in subduction zones: constraints from a laser ablation ICP-MS study of melt inclusions from Galunggung Volcano, Indonesia. Geochimica et Cosmochimica Acta, 65, 3147–3164.

de Hoog, J.C.M., Hattori, K.H., and Hoblitt, R.P. (2004) Oxidized sulfur-rich mafic magma at Mount Pinatubo, Philippines. Contributions to Mineralogy and Petrology, 146, 750–761.

DePaolo, D.J. (1981) Trace element and isotopic effects of combined wallrock assimilation and fractional crystallization. Earth and Planetary Science Letters, 53, 189–202.

Dowty, E. (1980) Crystal-chemical factors affecting the mobility of ions in minerals. American Mineralogist, 65, 174–182.

Duan, D.-F., and Jiang, S.-Y. (2018) Using apatite to discriminate synchronous ore-associated and barren granitoid rocks: A case study from the Edong metallogenic district, South China. Lithos, 310-311, 369–380.

Economos, R., Boehnke, P., and Burgisser, A. (2017) Sulfur isotopic zoning in apatite crystals: A new record of dynamic sulfur behavior in magmas. Geochimica et Cosmochimica Acta, 215, 387–403.

Edmonds, M., and Woods, A.W. (2018) Exsolved volatiles in magma reservoirs. Journal of Volcanology and Geothermal Research, 368, 13–30.

Edmonds, M., Aiuppa, A., Humphreys, M., Moretti, R., Giudice, G., Martin, R.S., Herd, R.A., and Christopher, T. (2010) Excess volatiles supplied by mingling of mafic magma at an andesite arc volcano. Geochemistry, Geophysics, Geosystems, 11(4). https://doi.org/10.1029/2009GC002781

Elburg, M., Vroon, P., van der Wagt, B., and Tchalikian, A. (2005) Sr and Pb isotopic composition of five USGS glasses (BHVO-2G, BIR-1G, BCR-2G, TB-1G, NKT-1G). Chemical Geology, 223, 196–207.

Farina, F., Stevens, G., and Villaros, A. (2012) Multi-batch, incremental assembly of a dynamic magma chamber: The case of the Peninsula pluton granite (Cape Granite Suite, South Africa). Mineralogy and Petrology, 106, 193–216.

Ferry, J.M., and Watson, E.B. (2007) New thermodynamic models and revised calibrations for the Ti-in-zircon and Zr-in-rutile thermometers. Contributions to Mineralogy and Petrology, 154, 429–437.

Gao, Y., Hoefs, J., Hellebrand, E., von der Handt, A., and Snow, J.E. (2007) Trace element zoning in pyroxenes from ODP Hole 735B gabbros: Diffusive exchange or synkinematic crystal fractionation? Contributions to Mineralogy and Petrology, 153, 429–442.

Griffin, W.L., Wang, X., Jackson, S.E., Pearson, N.J., O'Reilly, S.Y., Xu, X., and Zhou, X. (2002) Zircon chemistry and magma mixing, SE China: In-situ analysis of Hf isotopes, Tonglu and Pingtan igneous complexes. Lithos, 61, 237–269.

Gros, K., Słaby, E., Birski, Ł., Kozub-Budzyń, G., and Sláma, J. (2020) Geochemical evolution of a composite pluton: insight from major and trace element chemistry of titanite. Mineralogy and Petrology, 114(5), 375–401.

Guo, F., Nakamuru, E., Fan, W., Kobayoshi, K., and Li, C. (2007) Generation of palaeocene adakitic andesites by magma mixing; Yanji Area, NE China. Journal of Petrology, 48, 661–692.

Guo, F., Fan, W., Li, C., Zhao, L., Li, H., and Yang, J. (2012) Multi-stage crust–mantle interaction in SE China: Temporal, thermal and compositional constraints from the Mesozoic felsic volcanic rocks in eastern Guangdong-Fujian provinces. Lithos, 150, 62–84.

Harlov, D.E. (2015) Apatite: A fingerprint for metasomatic processes. Elements, 11, 171–176.

Harlov, D.E., and Förster, H.-J. (2003) Fluid-induced nucleation of (Y+REE)-phosphate minerals within apatite: Nature and experiment. Part II. Fluorapatite. American Mineralogist, 88, 1209–1229.

Harlov, D.E., Wirth, R., and Förster, H.-J. (2005) An experimental study of dissolution-reprecipitation in fluorapatite: Fluid infiltration and the formation of monazite. Contributions to Mineralogy and Petrology, 150, 268–286.

Ishlhara, S. (1977) The magnetite-series and ilmenite-series granitic rocks. Mining Geology, 27, 293–305.

Jugo, P.J., Luth, R.W., and Richards, J.P. (2005) An experimental study of the sulfur content in basaltic melts saturated with immiscible sulfide or sulfate liquids at 1300 °C and 10 GPa. Journal of Petrology, 46, 783–798.

Jung, S., Hoernes, S., Masberg, P., and Hoffer, E. (1999) The petrogenesis of some migmatites and granites (Central Damara Orogen, Namibia): Evidence for disequilibrium melting, wall-rock contamination and crystal fractionation. Journal of Petrology, 40, 1241–1269.

Kamenetsky, V.S., Wolfe, R.C., Eggins, S.M., Mernagh, T.P., and Bastrakov, E. (1999) Volatile exsolution at the Dinkidi Cu-Au porphyry deposit, Philippines: A melt-inclusion record of the initial ore-forming process. Geology, 27, 691–694.

Kim, Y., Konecke, B., Fiege, A., Simon, A., and Becker, U. (2017) An ab-initio study of the energetics and geometry of sulfide, sulfite, and sulfate incorporation into apatite: The thermodynamic basis for using this system as an oxybarometer. American Mineralogist, 102, 1646–1656.

Konecke, B.A., Fiege, A., Simon, A.C., Parat, F., and Stechern, A. (2017) Co-variability of S^{6+}, S^{4+}, and S^{2-} in apatite as a function of oxidation state: Implications for a new oxybarometer. American Mineralogist, 102, 548–557.

Ladenburger, S., Marks, M.A.W., Upton, B., Hill, P., Wenzel, T., and Markl, G. (2016) Compositional variation of apatite from rift-related alkaline igneous rocks of the Gardar Province, South Greenland. American Mineralogist, 101, 612–626.

Laurent, O., Zeh, A., Gerdes, A., Villaros, A., Gros, K., and Slaby, E. (2017) How do granitoid magmas mix with each other? Insights from textures, trace element and Sr-Nd isotopic composition of apatite and titanite from the Matok pluton (South Africa). Contributions to Mineralogy and Petrology, 172, 80.

Li, X.-H., Li, Z.-X., Wingate, M.T.D., Chung, S.-L., Liu, Y., Lin, G.-C., and Li, W.-X. (2006) Geochemistry of the 755Ma Mundine Well dyke swarm, northwestern Australia: Part of a Neoproterozoic mantle superplume beneath Rodinia? Precambrian Research, 146, 1–15.

Li, X.-H., Li, W.-X., Li, Q.-L., Wang, X.-C., Liu, Y., and Yang, Y.-H. (2010) Petrogenesis and tectonic significance of the ~850 Ma Gangbian alkaline complex in South China: Evidence from in situ zircon U-Pb dating, Hf-O isotopes and whole-rock geochemistry. Lithos, 114, 1–15.

Li, Z., Qiu, J.S., and Yang, X.M. (2014) A review of the geochronology and geochemistry of Late Yanshanian (Cretaceous) plutons along the Fujian coastal area of southeastern China: Implications for magma evolution related to slab break-off and rollback in the Cretaceous. Earth-Science Reviews, 128, 232–248.

Lisowiec, K., Slaby, E., and Förster, H.J. (2015) Polytopic Vector Analysis (PVA) modelling of whole-rock and apatite chemistry from the Karkonosze composite pluton (Poland, Czech Republic). Lithos, 230, 105–120.

Liu, Y. (1996) Simultaneous and precise determination of 40 trace elements in rock samples using ICP-MS. Geochimica, 25, 552–558 (in Chinese with English abstract).

Liu, Y.S., Hu, Z.C., Gao, S., Gunther, D., Xu, J., Gao, C.G., and Chen, H.H. (2008) In situ analysis of major and trace elements of anhydrous minerals by LA-ICP-MS without applying an internal standard. Chemical Geology, 257, 34–43.

Marks, M.A.W., Wenzel, T., Whitehouse, M.J., Loose, M., Zack, T., Barth, M., Worgard, L., Krasz, V., Eby, G.N., Stosnach, H., and others (2012) The volatile inventory (F, Cl, Br, S, C) of magmatic apatite: An integrated analytical approach. Chemical Geology, 291, 241–255.

Mavrogenes, J., and Blundy, J. (2017) Crustal sequestration of magmatic sulfur dioxide. Geology, 45, 211–214.

McDonough, W.F., and Sun, S.-S. (1995) The composition of the Earth. Chemical Geology, 120(3), 223–253.

Nash, W.P., and Crecraft, H.R. (1985) Partition coefficients for trace elements in silicic magmas. Geochimica et Cosmochimica Acta, 49, 2309–2322.

Nathwani, C.L., Loader, M.A., Wilkinson, J.J., Buret, Y., Sievwright, R.H., and Hollings, P. (2020) Multi-stage arc magma evolution recorded by apatite in volcanic

rocks. Geology, 48, 323–327.

Oppenheimer, C., Scaillet, B., and Martin, R.S. (2011) Sulfur Degassing from Volcanoes: Source Conditions, Surveillance, Plume Chemistry and Earth System Impacts. Reviews in Mineralogy and Geochemistry, 73, 363–421.

Pan, Y., and Fleet, M.E. (2002) Compositions of the apatite-group minerals: Substitution mechanisms and controlling factors. Reviews in Mineralogy and Geochemistry, 48, 13–49.

Parat, F., and Holtz, F. (2004) Sulfur partitioning between apatite and melt and effect of sulfur on apatite solubility at oxidizing conditions. Contributions to Mineralogy and Petrology, 147, 201–212.

Parat, F., Dungan, M.A., and Streck, M.J. (2002) Anhydrite, pyrrhotite, and sulfur-rich apatite: Tracing the sulfur evolution of an Oligocene andesite (Eagle Mountain, CO, USA). Lithos, 64, 63–75.

Parat, F., Holtz, F., and Streck, M.J. (2011) Sulfur-bearing magmatic accessory minerals. Reviews in Mineralogy and Geochemistry, 73, 285–314.

Peng, G., Luhr, J.F., and McGee, J.J. (1997) Factors controlling sulfur concentrations in volcanic apatite. American Mineralogist, 82, 1210–1224.

Perugini, D., De Campos, C.P., Dingwell, D.B., Petrelli, M., and Poli, G. (2008) Trace element mobility during magma mixing: Preliminary experimental results. Chemical Geology, 256, 146–157.

Piccoli, P.M., and Candela, P.A. (2002) Apatite in igneous systems. Reviews in Mineralogy and Geochemistry, 48, 255–292.

Pokrovski, G.S., Borisova, A.Y., and Bychkov, A.Y. (2013) Speciation and transport of metals and metalloids in geological vapors. Reviews in Mineralogy and Geochemistry, 76, 165–218.

Prowatke, S., and Klemme, S. (2006) Trace element partitioning between apatite and silicate melts. Geochimica et Cosmochimica Acta, 70, 4513–4527.

Rae, D.A., Coulson, I.M., and Chambers, A.D. (1996) Metasomatism in the North Qôroq Centre, South Greenland: Apatite chemistry and rare-earth element transport. Mineralogical Magazine, 60, 207–220.

Richards, J.P. (2015) The oxidation state, and sulfur and Cu contents of arc magmas: Implications for metallogeny. Lithos, 233, 27–45.

Sasaki, A., and Ishihara, S. (1979) Sulfur isotopic composition of the magnetite-series and ilmenite-series granitoids in Japan. Contributions to Mineralogy and Petrology, 68, 107–115.

Sha, L.-K., and Chappell, B.W. (1999) Apatite chemical composition, determined by electron microprobe and laser-ablation inductively coupled plasma mass spectrometry, as a probe into granite petrogenesis. Geochimica et Cosmochimica Acta, 63, 3861–3881.

Sharma, K., Blake, S., Self, S., and Krueger, A.J. (2004) SO₂ emissions from basaltic eruptions, and the excess sulfur issue. Geophysical Research Letters, 31.

Słaby, E., Martin, H., Hamada, M., Śmigielski, M., Domonik, A., Götze, J., Hoefs, J., Hałas, S., Simon, K., Devidal, J.-L., and others (2012) Evidence in Archaean alkali feldspar megacrysts for high-temperature interaction with mantle fluids. Journal of Petrology, 53, 67–98.

Streck, M.J. (2008) Mineral textures and zoning as evidence for open system processes. Reviews in Mineralogy and Geochemistry, 69, 595–622.

Streck, M.J., and Dilles, J.H. (1998) Sulfur evolution of oxidized arc magmas as recorded in apatite from a porphyry copper batholith. Geology, 26, 523–526.

Sun, J.-F., Zhang, J.-H., Yang, J.-H., Yang, Y.-H., and Chen, S. (2019) Tracing magma mixing and crystal-melt segregation in the genesis of syenite with mafic enclaves: Evidence from in situ zircon Hf-O and apatite Sr-Nd isotopes. Lithos, 334-335, 42–57.

Taylor, R.Z. (2004) Are plutons assembled over millions of years by amalgamation from small magma chambers? GSA Today, 14, 4.

Teiber, H., Marks, M.A.W., Wenzel, T., Siebel, W., Altherr, R., and Markl, G. (2014) The distribution of halogens (F, Cl, Br) in granitoid rocks. Chemical Geology, 374-375, 92–109.

Tepper, J.H., and Kuehner, S.M. (1999) Complex zoning in apatite from the Idaho Batholith; a record of magma mixing and intracrystalline trace element diffusion. American Mineralogist, 84, 581–595.

Trotter, J.A., Williams, I.S., Barnes, C.R., Lécuyer, C., and Nicoll, R.S. (2008) Did cooling oceans trigger ordovician biodiversification? Evidence from conodont thermometry. Science, 321, 550–554.

Tu, X.L., Zhang, H., Deng, W.F., Ling, M.X., Liang, H.Y., Liu, Y., and Sun, W.D. (2011) Application of RESOlution in-situ laser ablation ICP-MS in trace element analyses. Geochimica, 40, 83–98 (in Chinese with English abstract).

Turner, J.S., and Campbell, I.H. (1986) Convection and mixing in magma chambers. Earth-Science Reviews, 23, 255–352.

Van Hoose, A.E., Streck, M.J., Pallister, J.S., and Wälle, M. (2013) Sulfur evolution of the 1991 Pinatubo magmas based on apatite. Journal of Volcanology and Geothermal Research, 257, 72–89.

Wallace, P.J., and Edmonds, M. (2011) The sulfur budget in magmas: Evidence from melt inclusions, submarine glasses, and volcanic gas emissions. Reviews in Mineralogy and Geochemistry, 73, 215–246.

Wang, L.-X., Ma, C.-Q., Zhang, C., Zhu, Y.-X., and Marks, M.A. (2018) Halogen geochemistry of I-and A-type granites from Jiuhuashan region (South China): Insights into the elevated fluorine in A-type granite. Chemical Geology, 478, 164–182.

Watson, E.B., and Green, T.H. (1981) Apatite/liquid partition coefficients for the rare earth elements and strontium. Earth and Planetary Science Letters, 56, 405–421.

Webster, J.D. (2004) The exsolution of magmatic hydrosaline chloride liquids. Chemical Geology, 210, 33–48.

Webster, J.D., and Piccoli, P.M. (2015) Magmatic apatite: A powerful, yet deceptive, mineral. Elements, 11, 177–182.

Webster, J.D., and Vivo, B.D. (2002) Experimental and modeled solubilities of chlorine in aluminosilicate melts, consequences of magma evolution, and implications for exsolution of hydrous chloride melt at Mt. Somma-Vesuvius. American Mineralogist, 87, 1046–1061.

Webster, J.D., Holloway, J.R., and Hervig, R.L. (1989) Partitioning of lithophile trace elements between H₂O and H₂O + CO₂ fluids and topaz rhyolite melt. Economic Geology, 84, 116–134.

Webster, J.D., Baker, D.R., and Aiuppa, A. (2018) Halogens in mafic and intermediate-silica content magmas. In D.E. Harlov and L. Aranovich, Eds., The Role of Halogens in Terrestrial and Extraterrestrial Geochemical Processes: Surface, Crust, and Mantle, p. 307–430. Springer.

Weis, D., Kieffer, B., Maerschalk, C., Pretorius, W., and Barling, J. (2005) High-precision Pb-Sr-Nd-Hf isotopic characterization of USGS BHVO-1 and BHVO-2 reference materials. Geochemistry, Geophysics, Geosystems, 6.

Whalen, J.B., Currie, K.L., and Chappell, B.W. (1987) A-type granites: Geochemical characteristics, discrimination and petrogenesis. Contributions to Mineralogy and Petrology, 95, 407–419.

Xia, X.-P., Cui, Z.-X., Li, W., Zhang, W.-F., Yang, Q., Hui, H., and Lai, C.-K. (2019) Zircon water content: reference material development and simultaneous measurement of oxygen isotopes by SIMS. Journal of Analytical Atomic Spectrometry, 34, 1088–1097.

Xu, X., Zhao, K., He, Z., Liu, L., and Hong, W. (2020) Cretaceous volcanic-plutonic magmatism in SE China and a genetic model. Lithos, 105728.

Yan, L.-L., He, Z.-Y., Klemd, R., Beier, C., and Xu, X.-S. (2020) Tracking crystal-melt segregation and magma recharge using zircon trace element data. Chemical Geology, 542, 119596.

Yang, Y.-H., Wu, F.-Y., Yang, J.-H., Chew, D.M., Xie, L.-W., Chu, Z.-Y., Zhang, Y.-B., and Huang, C. (2014) Sr and Nd isotopic compositions of apatite reference materials used in U-Th-Pb geochronology. Chemical Geology, 385, 35–55.

Yu, K., Liu, Y., Hu, Q., Ducea, M.N., Hu, Z., Zong, K., and Chen, H. (2018) Magma recharge and reactive bulk assimilation in enclave-bearing granitoids, Tonglu, South China. Journal of Petrology, 59, 795–824.

Zajacz, Z., Halter, W.E., Pettke, T., and Guillong, M. (2008) Determination of fluid/melt partition coefficients by LA-ICPMS analysis of co-existing fluid and silicate melt inclusions: Controls on element partitioning. Geochimica et Cosmochimica Acta, 72, 2169–2197.

Zellmer, G.F., Edmonds, M., and Straub, S.M. (2015) Volatiles in subduction zone magmatism. Geological Society, London, Special Publications, 410, 1–17.

Zeng, L.-P., Zhao, X.-F., Li, X.-C., Hu, H., and McFarlane, C. (2016) In situ elemental and isotopic analysis of fluorapatite from the Taocun magnetite-apatite deposit, Eastern China: Constraints on fluid metasomatism. American Mineralogist, 101, 2468–2483.

Zhang, C., Holtz, F., Ma, C.Q., Wolff, P.E., and Li, X.Y. (2012) Tracing the evolution and distribution of F and Cl in plutonic systems from volatile-bearing minerals: a case study from the Liujiawa pluton (Dabie orogen, China). Contributions to Mineralogy and Petrology, 164, 859–879.

Zhang, G.W., Guo, A.L., Wang, Y.J., Li, S.Z., Dong, Y.P., Liu, S.F., He, D.F., Cheng, S.Y., Lu, R.K., and Yao, A.P. (2013) Tectonics of South China continent and its implications. Science China Earth Sciences, 56, 1804–1828.

Zhang, L., Ren, Z.-Y., Xia, X.-P., Li, J., and Zhang, Z.-F. (2015) IsotopeMaker: A Matlab program for isotopic data reduction. International Journal of Mass Spectrometry, 392, 118–124.

Zhang, B., Guo, F., Zhang, X., Wu, Y., Wang, G., and Zhao, L. (2019) Early cretaceous subduction of Paleo-Pacific Ocean in the coastal region of SE China: Petrological and geochemical constraints from the mafic intrusions. Lithos, 334, 8–24.

Zhang, X., Guo, F., Zhang, B., Zhao, L., Wu, Y., Wang, G., and Alemayehu, M. (2020) Magmatic evolution and post-crystallization hydrothermal activity in the early Cretaceous Pingtan intrusive complex, SE China: Records from apatite geochemistry. Contributions to Mineralogy and Petrology, 175, 35.

Zhou, X.M., Sun, T., Shen, W., Shu, L., and Niu, Y. (2006) Petrogenesis of Mesozoic granitoids and volcanic rocks in south China: A response to tectonic evolution. Episodes, 26–33.

Endnote:

[1]Deposit item AM-21-107786, Online Materials. Deposit items are free to all readers and found on the MSA website, via the specific issue's Table of Contents (go to http://www.minsocam.org/MSA/AmMin/TOC/2021/Oct2021_data/Oct2021_data.html).